



The Decisive Role of Spin States and Spin Coupling in Dictating Selective O₂ Adsorption in Chromium(II) Metal–Organic Frameworks**

Reshma Jose,^[a] Srinivasu Kancharlapalli,^[b] Tapan K. Ghanty,^[b, c] Sourav Pal,^{*,[d, e]} and Gopalan Rajaraman^{*,[a]}

Abstract: The coordinatively unsaturated chromium(II)-based Cr₃[(Cr₄Cl)₃(BTT)₈]₂ (Cr–BTT; BTT³⁻ = 1,3,5-benzenetristetrazolate) metal–organic framework (MOF) has been shown to exhibit exceptional selectivity towards adsorption of O₂ over N₂/H₂. Using periodic density functional theory (DFT) calculations, we attempted to decipher the origin of this puzzling selectivity. By computing and analyzing the magnetic exchange coupling, binding energies, the partial density of states (pDOS), and adsorption isotherms for the pristine and gas-bound MOFs [(Cr₄(X)₄Cl)₃(BTT)₈]₃³⁻ (X=O₂, N₂, and H₂), we unequivocally established the role of spin states and spin coupling in controlling the gas selectivity. The computed geometries and gas adsorption isotherms are consistent with the earlier experiments. The binding of O₂ to the MOF follows

an electron-transfer mechanism resulting in a Cr^{III} superoxo species (O₂^{•-}) with a very strong antiferromagnetic coupling between the two centers, whereas N₂/H₂ are found to weakly interact with the metal center and hence only slightly perturb the associated coupling constants. Although the gas-bound and unbound MOFs have an S=0 ground state (GS), the nature of spin the configurations and the associated magnetic exchanges are dramatically different. The binding energy and the number of oxygen molecules that can favorably bind to the Cr center were found to vary with respect to the spin state, with a significant energy margin (47.6 kJ mol⁻¹). This study offers a hitherto unknown strategy of using spin state/spin couplings to control gas adsorption selectivity in MOFs.

Introduction

Owing to their fascinating properties such as structural and functional diversity, tunable pore size, and enormous surface area, metal–organic frameworks (MOFs), have tremendous

applications in gas storage,^[1–4] molecular separation,^[5–10] sensors,^[11–15] and catalysis.^[16–22] Though zeolites, covalent organic frameworks, and complex hydrides are available for gas separation applications,^[23,24] MOF-based separative systems have attracted wide attention due to their high selectivity as a result of their extensive chemical diversity and porous nature in comparison to other classical adsorbate systems.^[25] The microporous nature of MOFs enables systematic immobilization of the functional materials, which are envisaged as a practical promise for gas purification and separation applications at an industrial scale. Whilst several MOFs based on first-row transition metals are known for switchable magnetic characteristics under the influence of guest molecule,^[26,27] temperature,^[28,29] and pressure,^[30] there are only a few reports of high selectivity towards oxygen. The selective adsorption of oxygen over other gases that generate high purity oxygen (>99%) has applications in healthcare, oxy-fuel combustion,^[31] ozone generation, semiconductors, and other industries. This is a challenging task, as the separation of O₂/N₂ mixture is difficult due to the similarity in their physical properties,^[32] such as kinetic diameter, polarizability, and boiling point. The current industry standard is cryogenic separation, which demands high pressure, temperature and large infrastructure that escalate production costs. Thus, an alternative separation technique based on porous material is in high demand. Long et al. recently reported Cr₃[(Cr₄Cl)₃(BTT)₈]₂ (BTT³⁻ = 1,3,5-benzenetristetrazolate)^[33] MOF, which exhibits very high selectivity for oxygen over hydrogen and nitrogen. Despite the

[a] R. Jose, Prof. G. Rajaraman
Department of Chemistry
Indian Institute of Technology Bombay
Powai, Mumbai 400076 (India)
E-mail: rajaraman@chem.iitb.ac.in

[b] Dr. S. Kancharlapalli, Dr. T. K. Ghanty
Theoretical Chemistry Section
Bhabha Atomic Research Centre
Mumbai 400085 (India)

[c] Dr. T. K. Ghanty
Present address: Bio-Science Group
Bhabha Atomic Research Centre
Mumbai 400085 (India)

[d] Prof. S. Pal
Department of Chemistry
Indian Institute of Science Education and Research
Kolkata, Mohanpur, Nadia 741246 (India)
E-mail: s.pal@iiserkol.ac.in

[e] Prof. S. Pal
Department of Chemistry, Ashoka University, Sonapat, Haryana, 131029, India

**] A previous version of this manuscript has been deposited on a preprint server (<https://doi.org/10.33774/chemrxiv-2021-482v6>).

Supporting information for this article is available on the WWW under <https://doi.org/10.1002/chem.202104526>

structural similarity of this MOF to other metal ion MOFs reported, this shows high selectivity towards O₂ compared to N₂ and is currently one among the best MOFs for O₂ selective separations.^[33] While multiple factors can influence gas adsorption in MOFs, the origin of very high selectivity for O₂ is perplexing because structurally similar metal ion MOFs are unselective. Though the role of spin state and spin coupling in selective gas binding is not well studied in MOFs, there are reports on the magnetic separation of small molecules.^[34,35] The spin states based selectivity of gas in MOF^[36] needs to be addressed in detail.

Results and Discussion

In this work, we undertook detailed periodic DFT calculations^[37] to decipher the origin of the selectivity observed starting from the X-ray structure reported^[33] (Figure 1a). This methodology has proven to yield very good geometries for open-shell MOFs and has shown to yield a good numerical estimate of exchange coupling constants (J).^[38,39] Our earlier studies on [Mn₁₉] clusters reveal that the combination of PBE with plane-wave basis sets yields J values which are similar to the estimate obtained from

B3LYP employing Gaussian-type basis set.^[40] To further assess, we have performed a limited benchmarking on a model complex (Table S1 in the Supporting Information), which supports the view that PBE yields a better estimate, though the magnitude is overestimated. Further, the sign and as well as the ratio of J values (J_1/J_2) which are the governing factors in deciding the ground state, are similar to B3LYP. This benchmark and also literature precedent offers confidence in the methodology chosen.^[37,40,41]

Our starting point is the reported X-ray structure^[33] in which $[(Cr_4Cl)_3(BTT)_8]^{3-}$ is the repeating unit in our calculations, unless otherwise mentioned (Figures 1 and S1, for simplicity the unit cell formula is quoted throughout). We have then considered oxygen adsorption in each of the Cr sites leading to $[(Cr_4(O_2)_4Cl)_3(BTT)_8]^{3-}$ species where end-on Cr^{III}-O₂^{•-} superoxo species is formed.

The calculations on the O₂ bound MOF ($[(Cr_4(O_2)_4Cl)_3(BTT)_8]^{3-}$) yields the Cr–O, O–O distances and Cr–O–O angles as 1.815 Å, 1.283 Å and 125.7°, respectively, and this is in excellent agreement with neutron diffraction data of 1.84(±2) Å, 1.26(±2) Å and 129°(±2) reported. A shorter Cr–O distance found here in the end-on Cr^{III}-O₂^{•-} superoxo MOF structure suggests less steric crowding compared to the end-on

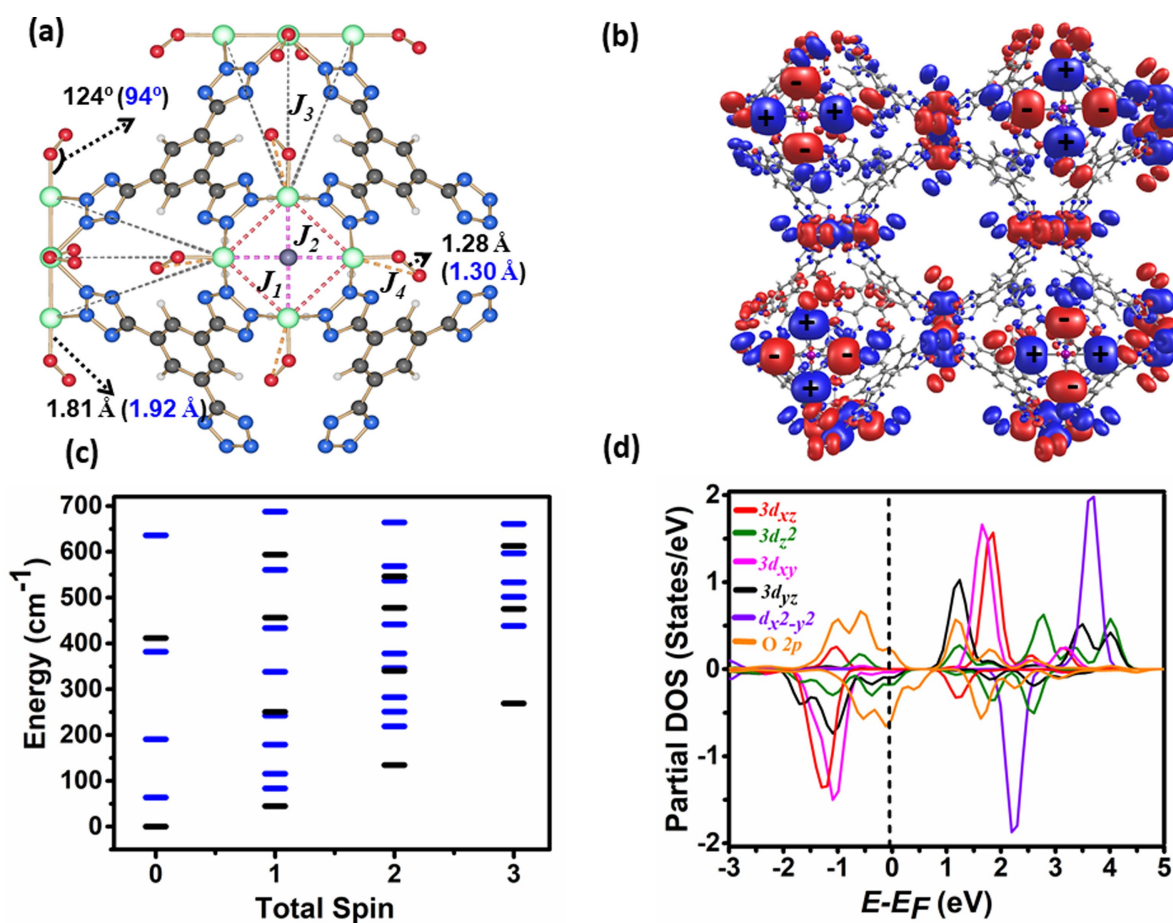


Figure 1. a) Geometry and representation of J_{1-4} bond parameters of GS (in black) and HS in $[(Cr_4(O_2)_4Cl)_3(BTT)_8]^{3-}$ MOF. (Cr: green, Cl: purple, N: blue, C: gray, H: white). b) GS spin-density plot of $[(Cr_4(O_2)_4Cl)_3(BTT)_8]^{3-}$. c) Estimated spin-state ladder based on DFT J values for O₂-bound (black) and unbound MOF. d) The partial DOS plot for the $[(Cr_4(O_2)_4Cl)_3(BTT)_8]^{3-}$ MOF.

$\text{Cr}^{\text{III}}\text{-O}_2^{\bullet-}$ superoxo biomimic models reported where the computed Cr–O distances are distinctly longer (1.965 \AA vs. $1.876(\pm 4)$ DFT vs. X-ray).^[42] The topological structure of $[(\text{Cr}_4\text{Cl})_3(\text{BTT})_8]^{3-}$ MOF has three J_5 ^[43] (Figure 1a) with J_1 describing the interaction between two Cr^{III} centers mediated by a BTT/ μ_4 -Cl bridge, J_2 by the μ_4 -Cl bridge and J_3 between two $\{\text{Cr}_4\}$ tetrameric units through the BTT^{3-} ligands. For the $[(\text{Cr}_4(\text{O}_2)_4\text{Cl})_3(\text{BTT})_8]^{3-}$ species, there is also an additional exchange between Cr^{III} and the $\text{O}_2^{\bullet-}$ superoxo species (J_4). Periodic DFT calculations for $[(\text{Cr}_4\text{Cl})_3(\text{BTT})_8]^{3-}$ ($[(\text{Cr}_4(\text{O}_2)_4\text{Cl})_3(\text{BTT})_8]^{3-}$) yield $J_1 = -25.8$ (-23.8) cm^{-1} , $J_2 = -41.8$ ($+3.4$) cm^{-1} and $J_3 = 0.3$ ($+0.5$) cm^{-1} ($J_4 = -1366$ cm^{-1}) with computed error in J s being negligible (Table S2). Computed O–O stretching frequencies on a $[(\text{Cr}_4\text{Cl})_3(\text{BTT})_8]^{3-}$ model is consistent with experiments (1206 vs. 1193 cm^{-1}).^[33] For the unbound MOF, the antiferromagnetic J_2 is the strongest, followed by J_1 and weakly ferromagnetic J_3 , and this trend is in line with the available magneto-structural correlations.^[43,44] The pseudo-Jahn–Teller elongation along the Cr–Cl bond results in dominant $d_{z^2}|p_z|d_{z^2}$ overlap leading to strong antiferromagnetic coupling. The J_3 interaction is mediated by longer tetrazolate bridges, and hence it is relatively weak. As exact diagonalization or Monte-Carlo simulations are not viable for this complex, we perform exact diagonalization with a smaller $\{\text{Cr}_4\}$ unit. This set of J values yield $S=0$ ground state (GS) for $\{\text{Cr}_4\}$ unit with another $S=0$ and $S=1$ excited states at 63.6 and 83.6 cm^{-1} higher, respectively, suggesting competing for AF interactions (Figure 1c). These values can not be validated as experimental magnetic data is not reported. Calculations yield the two-spin-up, two-spin-down Cr^{III} center as the lowest energy spin configuration (Figure S1 and Figure 1b) among all the spin configurations computed, where chromium has a spin density of ~ 2.9 (~ 3.8 on unbound MOF) and oxygen, ~ 0.9 . For O_2 bound MOF, all J values except J_2 and J_3 are estimated to be antiferromagnetic, with J_4 being the strongest, and this is also consistent with experiments.^[42,45] The Cr^{III} with unpaired electrons in d_{xy} , d_{xz} , and d_{yz} orbitals do not offer a direct overlap with the linear Cr–Cl–Cr bridge resulting in weak ferromagnetic J_2 exchange. Strong antiferromagnetic J_1 and J_4 enforce $S=0$ GS with alternate spin-up and -down in the $\{\text{Cr}_4\}$ unit with the $\text{O}_2^{\bullet-}$ spin antiferromagnetically coupled to each Cr center (see Figure S1 for the tetrameric unit), and this configuration is different from the unbound MOF $S=0$ state. Based on the atomic spin density, the unpaired electrons are found to be in the O–O (p^*) orbital with the distal oxygen found to have significant radical character (0.6), with the total unpaired electrons of ~ 0.93 detected on the oxygen molecule revealing a strong superoxo character. The nonlinear Cr–O–O angle of 126° facilitates strong overlap with the $\sigma^*(d_{z^2})$ and the axial π -donor Cl orbital destabilize the $d_{xz/yz}$ orbitals leading to, stronger overlap and hence strong binding as shown in the qualitative MO diagram derived (Figure S2). The qualitative MO diagram has been explained by considering monomeric chromium with a high-spin Cr^{III} center, whereas the DFT calculations on the MOF include individual Cr^{III} centers antiferromagnetically coupled to each other within the tetrameric unit leading to $S=0$ state.

The oxygen-binding was analyzed by the pDOS plot (Figure 1d), and near the Fermi level, the oxygen p-orbitals are found to mix strongly with the d-based orbitals of Cr ions. Particularly the $d_{x^2-y^2}$, and d_{z^2} orbitals are found close to the Fermi level, and if we compare the pDOS with unbound MOF (Figure 4a), reduction in the Cr d-orbital density is visible, suggesting oxidation of Cr ion as expected. Additionally, both the d_{z^2} and d_{yz} orbitals of Cr ions are found to split near the Fermi level suggesting mixing of these orbitals with oxygen leading to bonding/anti-bonding combinations as described in the qualitative MO diagram (Figure S2). Here, the pDOS plot is shown for a single chromium center that has a spin-down density. We have also plotted the total DOS for all four Cr d states, and as expected, this show two-spin-up, two-spin-down states (Figure S3). The binding energy (BE) computed by comparing the GS energy of $[(\text{Cr}_4\text{Cl})_3(\text{BTT})_8]^{3-}$ and $[(\text{Cr}_4(\text{O}_2)_4\text{Cl})_3(\text{BTT})_8]^{3-}$ in $\text{Cr}^{\text{III}}\text{-O}_2^{\bullet-}$ mode of binding is estimated to be -135.5 kJ mol^{-1} (per chromium site). This value is based on pure electronic energy and does not have corrections due to enthalpy and entropic terms. The $T\Delta S$ term for O_2 is reported to be 61 kJ mol^{-1} ^[46] at 298 K. After this correction, the binding energy in ΔG is -74.5 kJ mol^{-1} . This estimate agrees very well with experiments (-61 kJ mol^{-1}), offering confidence in the methodology chosen. This large exothermicity computed reveals the favorable formation of end-on $\text{Cr}^{\text{III}}\text{-O}_2^{\bullet-}$ superoxo species.^[33] The BE reported by us for a well characterized $\text{Cr}^{\text{III}}\text{-O}_2^{\bullet-}$ superoxo species $[\text{Cr}(14\text{-TMC})(\text{OO})(\text{Cl})]^+$ is -77 kJ mol^{-1} , which is significantly smaller compared to MOFs.^[42,45] In both cases, the -Cl ligand is found to be in the *trans* position, unveiling the importance of π -donor ligands in the stability of such transient species.^[47]

To understand the role of spin state in gas-binding, we computed the BE for various spin ladders estimated from the exchange interactions. If a higher excited $S=0$ state (LS (b)) is considered, the BE is found to differ by a few kJ mol^{-1} (Figure 2). For the high-spin (HS) state, the BE is relatively unfavorable (-87.9 kJ mol^{-1} per site with respect to the GS, LS (a)), and this is 47.6 kJ mol^{-1} (per site) higher compared to the GS, suggesting strong dependency of binding energy with respect to the spin states. The O_2 adsorption isotherm experimentally reported reveals that it is extraordinarily steep, reaching 7.01 wt% at 0.2 bar and saturates at 7.56 wt% at 1 bar, which is smaller than 11.3 wt% expected if all Cr ions are bound to O_2 . This approximately translates to O_2 binding in eight Cr centers among the 12 ions present in our adapted unit cell. In order to check the difference in BE with respect to the number of oxygen molecules to see if a cooperative binding is present, we estimated BE by varying the number of O_2 molecules from 2 (leaving ten chromium sites vacant) to 12 (~ 6.3 kJ per site), by even distribution of O_2 molecule to each tetrameric unit.

As we go from 2 to 8 (~ 6.3 kJ per site), BE becomes larger and larger, with the largest per site BE noted for eight oxygen molecules (-139.4 kJ mol^{-1}). The addition of further oxygen molecules tends to decrease the BE (2.5 kJ mol^{-1} per site), suggesting that 10 or 12 oxygen (full saturation point) binding is not very favorable, and this is consistent with experiments. The addition of oxygen beyond eight units tends to increase

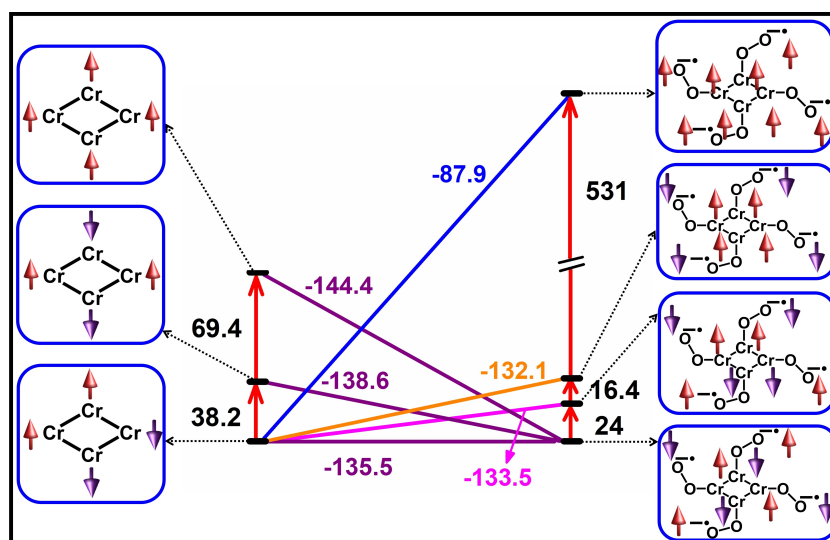


Figure 2. The energy level diagram depicts different spin states' comparative energies [kJ mol^{-1}] before and after oxygen binding.

the steric crowding at the tetrameric binding sites and also demands oxidation of all the Cr^{II} to Cr^{III} at the tetrameric unit cell. Further $\mu_4\text{-Cl}$ donation also diminishes in the fully oxidized tetrameric unit, as in the 12 O_2 models with the longest $\text{Cr}^{\text{III}}\text{-Cl}$ distance (Table S3). All these energy penalties diminish the binding energy. It is important to note here that the possibility of water reducing the overall performance cannot be ruled out, although experiments were performed under strict N_2 conditions.^[33]

For the HS state, different behavior is noted, with the most favorable BE found for six O_2 molecules with a much steeper energy penalty for additional oxygen bindings (12.8 kJ mol^{-1} per site). Again, spin state was found to dictate not only the BE preferences but also the number of oxygen molecules that can bind to the MOF in a favorable manner (Figure 3c). This suggests that switching of the spin state/exchange coupling is therefore expected to influence the selectivity considerably. To further understand the binding of oxygen, we have simulated the adsorption isotherms at 298 K and 0–4 bar using the RASPA suite (Figure 3a, b and Computational Details). To account for Cr–O covalent bond formation and BE difference among various spin states, we have performed further adsorption isotherm calculations using the starting geometry of $[(\text{Cr}_4\text{Cl})_3(\text{O}_2)_n(\text{BTT})_8]^{3-}$ ($n=2, 4, 6, 8, 10$ and 12 , (Figure 3a, see the Supporting Information for the corresponding equation used). The GS electronic configuration isotherm is very similar to the experimental curve.^[33] Moreover, from the simulated curve, it is clear that the HS state has a lesser tendency to bind oxygen compared to the antiferromagnetic $S=0$ GS, unveiling a strongly spin-state-dependent O_2 loading feature. The reason for unfavorable gas binding in the HS state ($S=8$ for a tetrameric $\text{Cr}^{\text{III}}\text{-O}_2^{\bullet-}$ unit) is partially due to the strong antiferromagnetic exchange between Cr^{III} and $\text{O}_2^{\bullet-}$ unit (J_4 value is $\sim 16.3 \text{ kJ mol}^{-1}$) and also due to unfavorable structural deformation in the HS state where the $\text{Cr}^{\text{III}}\text{-O}$ as well as O-O

bonds are much longer compared to the low-spin GS configuration (Figure 1a). Further calculations were performed for N_2 and H_2 adsorption, which yields BE of -35 and -16 kJ mol^{-1} , respectively. Both the values are significantly smaller than that found for O_2 , rationalizing the extraordinary selectivity for O_2 observed experimentally for this MOF. The binding of N_2/H_2 results in an $S=0$ GS similar to that of unbound MOF. The J values for MOF- N_2 (MOF- H_2) are estimated to be $J_1=-23.4$ (-27.3) cm^{-1} , $J_2=-34.1$ (-46.6) cm^{-1} , $J_3=-0.6$ (0.63) cm^{-1} , suggesting dominant antiferromagnetic coupling leading to a diamagnetic GS at lower temperatures. The N_2 is found to bind on end-on fashion with an estimated Cr–N distance of 2.19 \AA , whereas H_2 binds in a side-on fashion with an average Cr–H distance of 2.53 \AA and a Cr–H–H angle of $\sim 81^\circ$, suggesting a weak overlap with the metal ion; this is reaffirmed in the pDOS plot (Figure 4) where a very little overlap of Cr d-orbitals with the N_2/H_2 p/s-orbitals is noted. If we compare the d-based orbitals of Cr ion in the presence and absence of N_2/H_2 binding, it is clear that the d_{z^2} orbital is split, suggesting a weak $\text{Cr}^{\text{III}}\cdots\text{N}_2/\text{H}_2$ interaction with this orbital. To assess the energetic cost associated with the formation of $\{\text{Cr}^{\text{III}}\cdots\text{N}_2^{\bullet-}\}$ similar in line with oxygen binding, a coordinate scan analysis was performed by varying the N–N bond from 0.94 to 1.54 \AA . This reveals a partial formation of $\text{Cr}^{\text{III}}\text{-N}_2^{\bullet-}$ species at N–N $\sim 1.34 \text{ \AA}$, with an energy penalty of $\sim 150 \text{ kJ mol}^{-1}$ (per site), revealing the reason for very high selectivity towards O_2 (Figure 3d). Unlike O_2 , the isotherm obtained for N_2 shows a similar binding trend for HS and $S=0$ GS, suggesting that spin-state dependency in N_2 is absent (Figure 3b). A similar trend is also visible for the H_2 binding, unveiling the reason for the very high selectivity towards O_2 for this MOF.

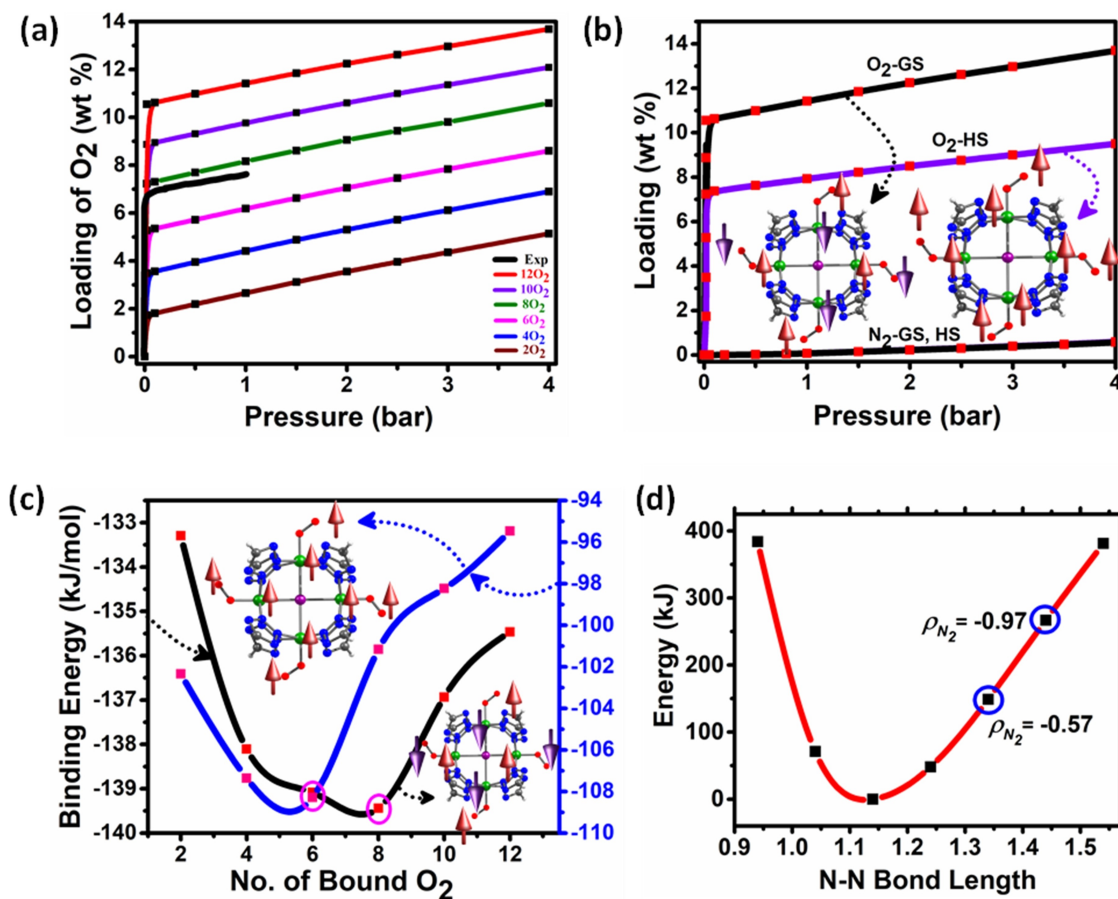


Figure 3. a) Computed adsorption isotherm for successive O₂ binding. b) Comparative adsorption isotherm for O₂ and N₂ in GS and HS states. c) Computed BE for successive addition of oxygen in GS (black, S=0) and HS (blue) states. d) Rigid scan of N–N bond distance in N₂-bound MOFs. Here the blue circled regions indicate the formation of radical at the N₂ moiety and corresponding spin density.

Conclusions

Using periodic DFT calculations, we have shown that spin state/exchange interaction plays a pivotal role in dictating the selectivity of gas adsorption in a chromium MOF. Among the O₂/N₂/H₂ gases studied, the electron-transfer mechanism adopted by O₂ leads to its strongly spin-state-dependent binding, whereas the other two gases do not exhibit such drastic variations. As the O₂/N₂-selective adsorption/desorption process has high commercial value, this study offers a hitherto unknown strategy of using spin-state/spin-coupling switching to control gas adsorption selectivity in MOFs.

Computational Details

All calculations were carried out by using periodic density functional methods^[48] implemented in the CP2k 2.4.0 suite. The Perdew–Burke–Ernzerhof (PBE)^[37] gradient-corrected, generalized gradient approximation (GGA) was used to describe the exchange–correlation functional, and DZVP-MOLOPT-GTH (valence double zeta (ζ) plus polarization, molecularly optimized, Goedecker–Teter–Hutter) basis set for atoms (H, C, O, N, Cl) and DZVP-MOLOPT-SR-GTH for Chromium atom by incorporating the short-range forces

with Gaussian-augmented plane wave (GAPW) approach with a kinetic energy cutoff of 400 Ry. The Grimme's D2 correction (DFT–D2) was used to account for the dispersion interactions. We have also performed calculations using D3 dispersion correction, which yields very similar geometries, binding energies, and J values (Table S4). The J values were calculated by using the non-spin projected formula. The boundary conditions $a=b=c$, which is set as 18.6695 Å. The PBE functional with the plane-wave basis set is shown to offer less delocalization, and this improves the numerical estimate of J compared to hybrid B3LYP functional.

Adsorption isotherms were simulated through the Grand Canonical Monte Carlo technique as implemented in the RASPA software.^[50] The Lennard–Jones (LJ) parameters for the considered framework atoms were taken from Universal Force Field (UFF),^[51] and Lorentz–Berthelot mixing rules are used to calculate the cross interactions. Both N₂ and O₂ molecules were modeled using the TraPPE force field.^[52] We used 50 000 equilibration cycles and 50 000 production cycles for each simulation and considered insertion, deletion, translation, and rotation moves. Since the chemisorption of O₂ cannot be modeled using the GCMC technique, we considered initial framework structures with the different number of O₂ molecules chemisorbed, and the corresponding weight of O₂ is also considered for plotting the O₂ loading in addition to the loading obtained from the GCMC simulations.

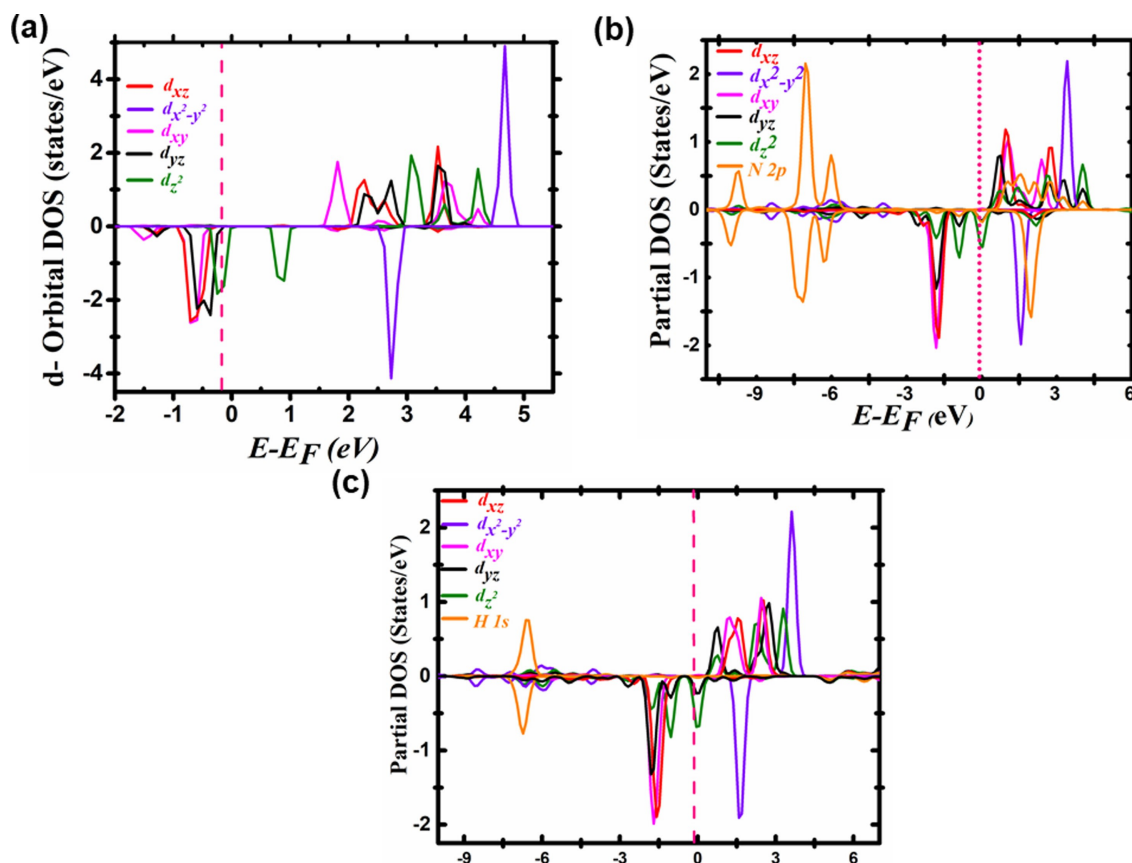


Figure 4. The partial DOS for a) unbound, b) N_2 -bound, and c) H_2 -bound MOFs; the Fermi energy levels are marked with pink dotted lines.

Conflict of Interest

There are no conflicts to declare.

Data Availability Statement

The data that support the findings of this study are available in the supplementary material of this article.

Keywords: chromium superoxo · DFT calculations · gas adsorption · MOFs · spin-state calculations

- [1] V. Y. Mao, P. J. Milner, J. H. Lee, A. C. Forse, E. J. Kim, R. L. Siegelman, C. M. McGuirk, L. B. Porter-Zasada, J. B. Neaton, J. A. Reimer, *Angew. Chem. Int. Ed.* **2020**, *59*, 19468–19477; *Angew. Chem.* **2020**, *132*, 19636–19645.
- [2] E. J. Kim, R. L. Siegelman, H. Z. Jiang, A. C. Forse, J.-H. Lee, J. D. Martell, P. J. Milner, J. M. Falkowski, J. B. Neaton, J. A. Reimer, *Science* **2020**, *369*, 392–396.
- [3] B. M. Connolly, D. G. Madden, A. E. Wheatley, D. Fairen-Jimenez, *J. Am. Chem. Soc.* **2020**, *142*, 8541–8549.
- [4] C. Nagaraja, R. Haldar, T. K. Maji, C. Rao, *Cryst. Growth Des.* **2012**, *12*, 975–981.
- [5] Q. Qian, P. A. Asinger, M. J. Lee, G. Han, K. Mizrahi Rodriguez, S. Lin, F. M. Benedetti, A. X. Wu, W. S. Chi, Z. P. Smith, *Chem. Rev.* **2020**, *120*, 8161–8266.
- [6] L. Liu, Z. Yao, Y. Ye, Y. Yang, Q. Lin, Z. Zhang, M. O’Keeffe, S. Xiang, *J. Am. Chem. Soc.* **2020**, *142*, 9258–9266.
- [7] D. E. Jaramillo, D. A. Reed, H. Z. Jiang, J. Oktawiec, M. W. Mara, A. C. Forse, D. J. Lussier, R. A. Murphy, M. Cunningham, V. Colombo, *Nat. Mater.* **2020**, *19*, 517–521.
- [8] Q. Hou, S. Zhou, Y. Wei, J. r. Caro, H. Wang, *J. Am. Chem. Soc.* **2020**, *142*, 9582–9586.
- [9] H. Wang, Z. Shi, J. Yang, T. Sun, B. Rungtaweevoranit, H. Lyu, Y. B. Zhang, O. M. Yaghi, *Angew. Chem. Int. Ed.* **2021**, *133*, 3459–3463.
- [10] W. Xu, O. M. Yaghi, *ACS Cent. Sci.* **2020**, *6*, 1348–1354.
- [11] X. Z. Wang, X. Y. Mao, Z. Q. Zhang, R. Guo, Y. Y. Zhang, N. J. Zhu, K. Wang, P. P. Sun, J. Z. Huo, X. R. Wang, *Inorg. Chem.* **2020**, *59*, 2910–2922.
- [12] L.-T. Zhang, Y. Zhou, S.-T. Han, *Angew. Chem. Int. Ed.* **2020**; *Angew. Chem.* **2021**, *133*, 15320–15340.
- [13] J. Li, S. Yuan, J. S. Qin, J. Pang, P. Zhang, Y. Zhang, Y. Huang, H. F. Drake, W. R. Liu, H. C. Zhou, *Angew. Chem. Int. Ed.* **2020**, *59*, 9319–9323; *Angew. Chem.* **2020**, *132*, 9405–9409.
- [14] K. Jayaramulu, R. P. Narayanan, S. J. George, T. K. Maji, *Inorg. Chem.* **2012**, *51*, 10089–10091.
- [15] L.-A. Cao, M.-S. Yao, H.-J. Jiang, S. Kitagawa, X.-L. Ye, W.-H. Li, G. Xu, *J. Mater. Chem. A* **2020**, *8*, 9085–9090.
- [16] S. Dutta, N. Kumari, S. Dubbu, S. W. Jang, A. Kumar, H. Ohtsu, J. Kim, S. H. Cho, M. Kawano, I. S. Lee, *Angew. Chem. Int. Ed.* **2020**, *132*, 3444–3450.
- [17] E. Tiburcio, R. Greco, M. Mon, J. Ballesteros-Soberanas, J. S. Ferrando-Soria, M. López-Haro, J. C. Hernández-Garrido, J. Oliver-Meseguer, C. Marini, M. Boronat, *J. Am. Chem. Soc.* **2021**, *143*, 2581–2592.
- [18] M. Li, J. Chen, W. Wu, Y. Fang, S. Dong, *J. Am. Chem. Soc.* **2020**, *142*, 15569–15574.
- [19] R. A. Peralta, M. T. Huxley, J. D. Evans, T. Fallon, H. Cao, M. He, X. S. Zhao, S. Agnoli, C. J. Sumby, C. J. Doonan, *J. Am. Chem. Soc.* **2020**, *142*, 13533–13543.
- [20] Z. Jiang, X. Xu, Y. Ma, H. S. Cho, D. Ding, C. Wang, J. Wu, P. Oleynikov, M. Jia, J. Cheng, *Nature* **2020**, *586*, 549–554.

- [21] C. A. Trickett, T. M. O. Popp, J. Su, C. Yan, J. Weisberg, A. Huq, P. Urban, J. Jiang, M. J. Kalmutzki, Q. Liu, J. Baek, M. P. Head-Gordon, G. A. Somorjai, J. A. Reimer, O. M. Yaghi, *Nat. Chem.* **2019**, *11*, 170–176.
- [22] J. Baek, B. Rungtaweevoranit, X. Pei, M. Park, S. C. Fakra, Y.-S. Liu, R. Mathew, S. A. Alshimiri, S. Alshehri, C. A. Trickett, G. A. Somorjai, O. M. Yaghi, *J. Am. Chem. Soc.* **2018**, *140*, 18208–18216.
- [23] R.-B. Lin, S. Xiang, H. Xing, W. Zhou, B. Chen, *Coord. Chem. Rev.* **2019**, *378*, 87–103.
- [24] H. Li, K. Wang, Y. Sun, C. T. Lollar, J. Li, H.-C. Zhou, *Mater. Today* **2018**, *21*, 108–121.
- [25] R. Haldar, T. K. Maji, *CrystEngComm* **2013**, *15*, 9276–9295.
- [26] M. D. Allendorf, M. E. Foster, F. Leonard, V. Stavila, P. L. Feng, F. P. Doty, K. Leong, E. Y. Ma, S. R. Johnston, A. A. Talin, *J. Phys. Chem. Lett.* **2015**, *6*, 1182–1195.
- [27] P. D. Southon, L. Liu, E. A. Fellows, D. J. Price, G. J. Halder, K. W. Chapman, B. Moubaraki, K. S. Murray, J.-F. Létard, C. J. Kepert, *J. Am. Chem. Soc.* **2009**, *131*, 10998–11009.
- [28] M. Wriedt, A. A. Yakovenko, G. J. Halder, A. V. Prosvirin, K. R. Dunbar, H.-C. Zhou, *J. Am. Chem. Soc.* **2013**, *135*, 4040–4050.
- [29] J. Park, D. Yuan, K. T. Pham, J.-R. Li, A. Yakovenko, H.-C. Zhou, *J. Am. Chem. Soc.* **2012**, *134*, 99–102.
- [30] S. Yuan, X. Sun, J. Pang, C. Lollar, J.-S. Qin, Z. Perry, E. Joseph, X. Wang, Y. Fang, M. Bosch, *Joule* **2017**, *1*, 806–815.
- [31] A. Kather, G. Scheffknecht, *Naturwissenschaften* **2009**, *96*, 993–1010.
- [32] J.-R. Li, R. J. Kuppler, H.-C. Zhou, *Chem. Soc. Rev.* **2009**, *38*, 1477–1504.
- [33] E. D. Bloch, W. L. Queen, M. R. Hudson, J. A. Mason, D. J. Xiao, L. J. Murray, R. Flacau, C. M. Brown, J. R. Long, *Angew. Chem. Int. Ed.* **2016**, *55*, 8605–8609; *Angew. Chem.* **2016**, *128*, 8747–8751.
- [34] Y. Xianyu, Y. Dong, Z. Zhang, Z. Wang, W. Yu, Z. Wang, Y. Chen, *Biosens. Bioelectron.* **2020**, *155*, 112106.
- [35] Y. Hu, X. Guo, H. Wang, Q. Luo, Y. Song, E. Song, *ACS Appl. Bio Mater.* **2020**, *3*, 2651–2657.
- [36] W. Kosaka, Z. Liu, J. Zhang, Y. Sato, A. Hori, R. Matsuda, S. Kitagawa, H. Miyasaka, *Nat. Commun.* **2018**, *9*, 1–9.
- [37] J. N. Harvey, *Annu. Rep. Prog. Chem. Sect. C* **2006**, *102*, 203–226.
- [38] S. Schwalbe, K. Trepte, G. Seifert, J. Kortus, *Phys. Chem. Chem. Phys.* **2016**, *18*, 8075–8080.
- [39] S. O. Odoh, C. J. Cramer, D. G. Truhlar, L. Gagliardi, *Chem. Rev.* **2015**, *115*, 6051–6111.
- [40] R. Nabi, G. Rajaraman, *Chem. Commun.* **2019**, *55*, 8238–8241.
- [41] E. Ruiz, T. Cauchy, J. Cano, R. Costa, J. Tercero, S. Alvarez, *J. Am. Chem. Soc.* **2008**, *130*, 7420–7426.
- [42] A. Ansari, P. Jayapal, G. Rajaraman, *Angew. Chem. Int. Ed.* **2015**, *127*, 574–578.
- [43] E. Ruiz, J. Cano, S. Alvarez, P. Alemany, *J. Comput. Chem.* **1999**, *20*, 1391–1400.
- [44] M. D. Fryzuk, D. B. Leznoff, S. J. Rettig, R. C. Thompson, *Inorg. Chem.* **1994**, *33*, 5528–5534.
- [45] J. Cho, J. Woo, W. Nam, *J. Am. Chem. Soc.* **2010**, *132*, 5958–5959.
- [46] J. K. Nørskov, J. Rossmeisl, A. Logadottir, L. Lindqvist, J. R. Kitchin, T. Bligaard, H. Jonsson, *J. Phys. Chem. B* **2004**, *108*, 17886–17892.
- [47] A. S. Rosen, M. R. Mian, T. Islamoglu, H. Chen, O. K. Farha, J. M. Notestein, R. Q. Snurr, *J. Am. Chem. Soc.* **2020**, *142*, 4317–4328.
- [48] D. Nazarian, P. Ganesh, D. S. Sholl, *J. Mater. Chem. A* **2015**, *3*, 22432–22440.
- [49] A. Bencini, F. Totti, *J. Chem. Theory Comput.* **2009**, *5*, 144–154.
- [50] D. Dubbeldam, S. Calero, D. E. Ellis, R. Q. Snurr, *Mol. Simul.* **2016**, *42*, 81–101.
- [51] A. K. Rappé, C. J. Casewit, K. Colwell, W. A. Goddard III, W. M. Skiff, *J. Am. Chem. Soc.* **1992**, *114*, 10024–10035.
- [52] J. J. Potoff, J. I. Siepmann, *AIChE J.* **2001**, *47*, 1676–1682.

Manuscript received: December 21, 2021

Accepted manuscript online: January 30, 2022

Version of record online: February 19, 2022